ACS NANO

www.acsnano.org

ARTICLE

Strong In-plane Magnetic Anisotropy in Semiconducting Monolayer $CoCl_2$

Samuel Kerschbaumer,* Sebastien Elie Hadjadj, Andrea Aguirre-Baños, Danilo Longo, Andrés Pinar Solé, Oleksandr Stetsovych, Adriana Elizabet Candia, Paula Angulo-Portugal, David Caldevilla, Fadi Choueikani, Martina Corso, David Serrate, Jorge Lobo-Checa, Pavel Jelínek, Maxim Ilyn, and Celia Rogero*

Cite This: *ACS Nano* 2025, 19, 20693−20701

Read Online

ACCESS | Metrics & More | Article Recommendations | Supporting Information

ABSTRACT: **Transition-metal dihalides (TMDH) are emerging as a highly promising class of 2D magnetic materials due to their simplicity, stability, and compatibility with nanofabrication techniques. In this work, we explore the structural, electronic, and magnetic properties of monolayer $CoCl_2$ grown epitaxially on Au(111) using a multitechnique approach. Our results reveal that epitaxial $CoCl_2$ exhibits ferromagnetic order below 24 K with strong in-plane magnetic anisotropy, setting it apart from other TMDH materials. Additionally, we identify in-gap states arising from the $CoCl_2$−Au(111) interface, which provide insights into its electronic behavior. These findings position $CoCl_2$ as a versatile 2D material for spintronic applications and nanoscale devices, bridging the gap between fundamental research and real-world technological solutions.**

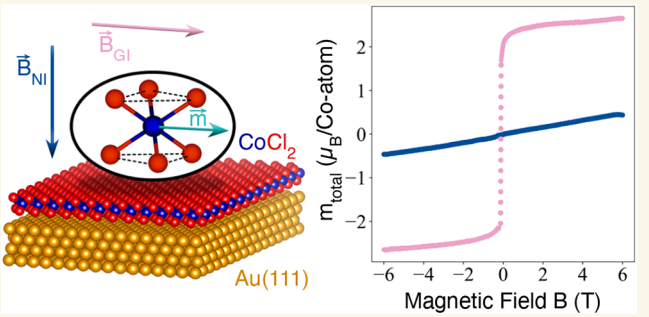

KEYWORDS: *2D ferromagnetic materials, van der Waals semiconductors, monolayer $CoCl_2$, in-plane magnetism, magnetic thin films, transition-metal dihalides*

The ever-growing interest to substitute silicon with more economic and efficient nanomaterials in the market for next-generation electronics has led to the discovery and characterization of many new 2D materials.[1−5] Magnetic 2D materials have gained increasing interest, due to their potential applications as ultrathin barriers for spin-polarized tunneling in devices or for fabricating superconductor-ferromagnet heterostructures.[6−9] Numerous theoretical calculations predict magnetic order in various 2D materials,[10−14] but only a few have been experimentally confirmed at the single-layer limit.[4,15−19] Since the first experimental demonstration of CrI_3[4] and $Cr_2Ge_2Te_6$,[15] other materials have been investigated,[8,14] including transition-metal dichalcogenides (TMDC) and transition-metal dihalides (TMDH).[20,21] These 2D magnets are considered valuable building blocks for inducing proximity magnetization effects in van der Waals heterostructures. A common technique to obtain monolayer samples is by exfoliating bulk single crystals. It has been shown that materials in the TMDH family can be synthesized by sublimating stoichiometric powder onto single crystal substrates maintained at relatively low temperatures (around 100 °C), a key advantage for compatibility with a wide range of nanofabrication techniques.[22,23]

Monolayers of TMDH compounds have a 1T crystal structure where two halogen layers are enclosing a triangular lattice of transition-metal atoms, creating an octahedral coordination[10] (Figure S1). The crystal field from the halogens splits the d-orbitals, thereby influencing the magnetic behavior. The Goodenough−Kanamori−Anderson (GKA) rules[24] describe superexchange interactions in these wide-bandgap semiconductors, where indirect hopping between metal atoms determines magnetic ordering with antiferromagnetic (AFM) or ferromagnetic (FM) arrangement, depending on the orbital occupation. In recent years, collinear and noncollinear FM ordering with relatively weak magnetic anisotropy have been reported in monolayers of Ni and Fe TMDH compounds grown on Au(111).[16,17,19] In this work, we present a comprehensive multitechnique investigation that provides clear evidence of the structural, electronic, chemical, and

Received: February 6, 2025
Revised: May 23, 2025
Accepted: May 23, 2025
Published: May 30, 2025

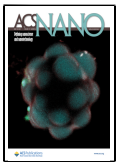

https://doi.org/10.1021/acsnano.5c02175
ACS Nano 2025, 19, 20693−20701

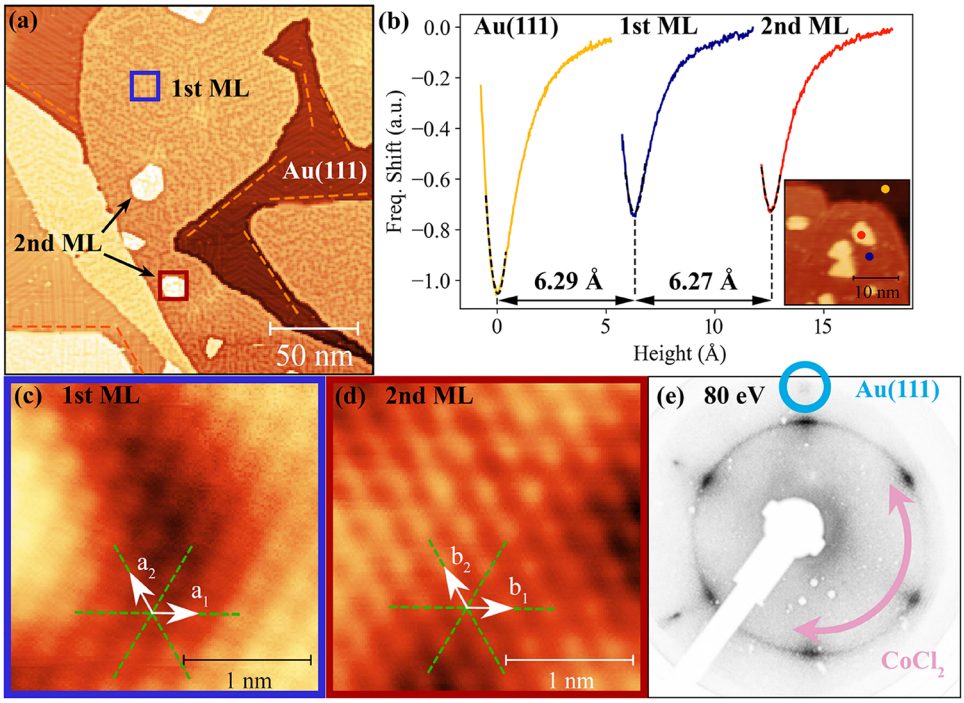

Figure 1. (a) Large-scale STM image showing the growth of first-layer $CoCl_2$ islands and the initiation of second layer growth in the sub-ML coverage regime. The hexagonal symmetry of the first layer is suggested by the straight edges marked by orange dashed lines. (b) Height measurements via Z-spectroscopy with a CO functionalized tip. Atomic resolution of (c) the first and (d) the second layer shown on the same absolute color scale. All unit vectors (a_1, a_2, b_1, b_2) align with the Au(111) lattice (green dashed lines). The ring-shaped $CoCl_2$ diffraction pattern (e) with increased intensity along the gold direction suggests the presence of multiple rotational domains that preferentially align with the Au(111) lattice. (a) U = 1.3 V, I_t = 30 pA, 210 nm, nominal coverage = 0.8 ML, (c) U = 0.2 V, I_t = 27 pA, 5 nm, $a_1 = a_2$ = 3.6 ± 0.1 Å, (d) U = 0.8 V, I_t = 20 pA, 5 nm, $b_1 = b_2$ = 3.6 ± 0.1 Å, (e) LEED: 80 eV.

magnetic properties of thin films of the semiconducting van der Waals material $CoCl_2$ grown on Au(111). This material turns out to exhibit a very strong magnetic anisotropy, which contrasts with the properties of Ni and Fe compounds. Our study offers a detailed exploration of how $CoCl_2$ behaves at the monolayer level, revealing its potential in advanced nanoscale applications and offering insights into the underlying physics.

RESULTS

Analogous to $FeCl_2$ and $NiCl_2$,[19] $CoCl_2$ grows in a layer-by-layer fashion when deposited onto Au(111). Figure 1a shows the growth of $CoCl_2$ in scanning tunneling microscopy (STM) in the submonolayer (sub-ML) regime. The large-scale topography shows three regions: the herringbone reconstruction of clean Au(111), large first-layer islands, and small second-layer islands growing on top. The first-layer islands have the ability to seamlessly overgrow step edges as a continuous film (see also Figure S5), indicating weak interaction with the substrate and a high degree of flexibility and stability arising from strong bonds within the layer. Another indicator is the preservation of the herringbone reconstruction, which remains unaffected beneath the partially transparent material. Notably, the second layer is observed before the gold surface is fully covered. This implies that thermally driven motion on top of the first layer is reduced compared with the Au(111) substrate.

$CoCl_2$ exhibits a regular ABC stacking order in bulk with parallel aligned atomic rows between the layers, so we expect a similar behavior when growing this material on Au(111).[25] This can be seen in the second-layer islands, which appear consistently aligned with the first-layer island (Figures 1 and S5). In contrast, first-layer islands can have any orientation with respect to Au(111), again revealing the low TMDH/Au(111) interaction.[26,27] The diffraction pattern of a LEED measurement in Figure 1e is an average of all periodic structures in the topmost few layers of the sample (highly surface sensitive). Since the Au(111) crystal has a fixed orientation and hexagonal symmetry, it creates only one set of hexagonal diffraction spots at a fixed position in reciprocal space. A ring-shaped LEED pattern on the other hand indicates that the atomic rows can have any orientation relative to the substrate. Low-energy electron diffraction (LEED) (Figure 1e) reveals a slight preference aligning with the close-packed Au(111) directions, evident from the enhanced intensity in the ring-shaped pattern. An increase in coverage shows a weakening of the Au(111) spots and no appearance of new diffraction spots (see Θ = 3.2 ML, Figure S11), indicating that the $CoCl_2$ structure remains the same.

According to high-resolution STM images, the lateral lattice constant for the first and second layers (Figure 1c,d) is 3.6 ± 0.1 Å (determination in Figure S4), which is in good agreement with the 3.54 Å predicted in literature.[10] To obtain the interlayer distances, Z-spectroscopy via noncontact AFM with a CO functionalized tip was performed (Figure 1b). By approaching the tip while measuring the frequency shift, the point of equilibrium between attractive and repulsive forces is identified, enabling the determination of the height between layers. A step height of approximately 6.3 Å is obtained for the first and second layers, close to the 5.93 Å predicted for $CoCl_2$'s 1T structure in literature.[28] 1T-$CoCl_2$ consists of three atomic planes stacked in a Cl−Co−Cl manner (Figure S1). Since X-ray photoelectron spectroscopy (XPS) measurements

https://doi.org/10.1021/acsnano.5c02175
ACS Nano 2025, 19, 20693−20701

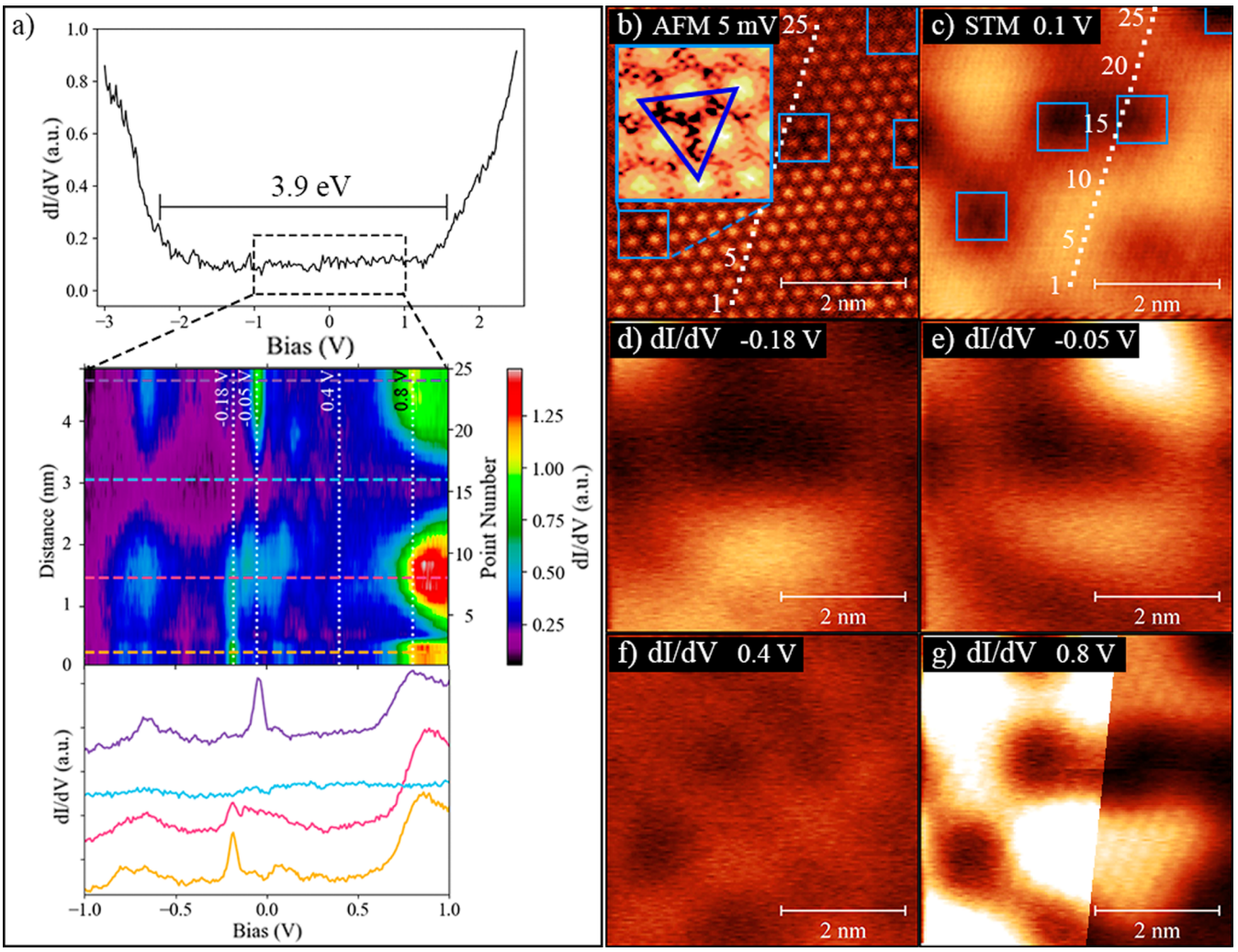

Figure 2. (a) dI/dV spectrum showing the onset of the valence and conduction band of $CoCl_2$. Twenty-five dI/dV spectra measured within the bias range from −1 to +1 V are shown in the inset. Four representative spectra are shown below the color map, corresponding to the color-coded horizontal lines (point numbers 2, 8, 16, 24). (b, c) AFM and STM images indicating the positions of the 25 dI/dV measurements. dI/dV maps at constant current (I_t = 10 pA); (d) −0.18 V, (e) −0.05 V, (f) 0.4 V, and (g) 0.8 V analyze the spatial distribution of the in-gap states within a ±5 mV range on the same absolute color scale (in (g) left: same color scale; right: adjusted color scale for improved visualization). The blue squares in (b) and (c) indicate areas with structural alterations from the normal atomic resolution with hexagonal symmetry causing a contrast depletion centered between 3 top-layer Cl atoms (blue triangle).

revealed a Co to Cl ratio of 1:2 and consistent peak positions across different coverages (see Figure S11), we confirm regular and stoichiometric bulk-like growth.[29] Theoretical calculations for the closely related $FeCl_2$ have shown that the 1T configuration is the most stable and energetically favorable.[30,31]

Figure 2a shows a typical U-shaped differential conductance curve, measured on the first $CoCl_2$ layer, which suggests an ≈3.9 eV band gap.[31−33] Closer inspection of the bias range from −1 to 1 V reveals states appearing within the band gap of $CoCl_2$. Figure 2a (inset) shows an STS color map obtained by measuring point spectroscopy on 25 consecutive locations along the dotted line (Figure 2b,c). Four selected point spectra measured at different positions (point numbers: 2, 8, 16, and 24) illustrate the spectral changes of the states in this reduced voltage range. To better visualize the spatial distribution of these in-gap states, dI/dV maps (V_{Mod} = 5 mV) were measured at four bias values of interest marked by the white, dotted, vertical lines in Figure 2a. dI/dV maps measured at these bias voltages shown in Figure 2d−g directly display the spatial distribution of these states on the surface. In this direct intensity comparison, the map at 0.4 V in Figure 2f shows almost no contrast, as no states are visible across the entire range of the point spectra (see 0.4 V in the color map). Figure 2d,e,g exhibits modulation in the spatial distribution of the states at −0.18, −0.05, and 0.80 V, respectively.

The emergence of these states is clearly position-dependent and does not follow the atomic periodicity of the layer, visible in Figure 2c. Upon closely analyzing the atomic resolution in the AFM image in Figure 2b (inset), a contrast depletion centered between three top-layer Cl atoms is visible (blue triangle in the inset, also marked by blue squares at other sites in the image). This depletion coincides with the darker regions observed in STM (c) indicating areas with a reduced local density of states (LDOS). Note the absence of in-gap states in the proximity of these reduced LDOS sites across the entire bias range. Locally stronger interactions between a bottom layer Cl atom and a Au(111) atom due to their incommensurate lattices or subsurface defects could be respo this feature. The large-scale electronic contrast observed in STM measurements of the second monolayer is notably

https://doi.org/10.1021/acsnano.5c02175
ACS Nano 2025, 19, 20693−20701

weaker (see Figure 1c,d: same absolute color scale). Nevertheless, the in-gap states can be clearly observed in the STS spectra measured in the bilayer (see Figure S7).

To analyze surface state dispersions, a series of dI/dV maps was measured over a bias range from −0.45 to +0.50 V on both clean Au(111) and $CoCl_2$-covered regions (Figure 3).

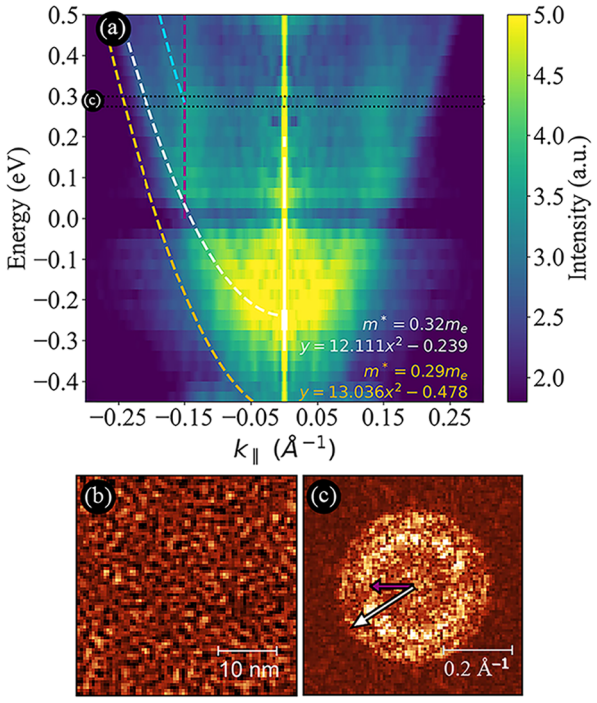

Figure 3. (a) Dispersion relation of $CoCl_2$ on Au(111) extracted from the dI/dV maps measured in the bias range from −0.45 to +0.5 V. The white parabola represents the dispersion of the interface state on the $CoCl_2$-covered region, which is shifted to higher energies compared with the pristine Au(111) surface. The orange parabola, overlaid schematically, indicates the dispersion of the clean Au(111) surface state (Figure S10) and the light blue dashed line shows a second additional dispersive feature we were not able to identify. A nondispersive feature, present only in the positive bias voltage range, that Schouteden et al.[34] attributed to the Au(111) bulk states is marked by a violet dashed line. This nondispersive feature is found at 0.15 ± 0.01 Å^{-1}, which corresponds to a 21 Å distance in real space (Figure S9). The horizontal black dotted line (labeled as (c) on the left side) corresponds to the energy range in the dispersion plot related to the Fourier transform shown in (c). (b) dI/dV map of $CoCl_2$ on Au(111) acquired at a sample bias of 0.3 V with a modulation amplitude of 5 mV. (c) Fourier transform of the real-space dI/dV map, highlighting two concentric rings as indicated by the color-coded arrows.

Applying a Fourier transform to the dI/dV maps measured at different bias voltages allows for the visualization and characterization of the parabolic dispersion of the surface state. The $CoCl_2$ film modifies the surface state of the Au(111) substrate, typically located at −0.5 V,[34] by shifting it to higher energies. This shift occurs because the $CoCl_2$ layer acts as a barrier, compressing the Au(111) surface state into a more confined space and thereby raising its energy. This is shown in Figure 3a, where each energy shows the radial distribution of these states in k-space. Figure 3b,c shows the dI/dV map and its corresponding fast Fourier transformation (FFT) at 0.3 V. Note how the states marked by the white and violet dashed lines in Figure 3a are also visible in FFT (c-arrows). The experimental analysis follows previous work[34,35] and is detailed in Figure S8. The dispersion relation for these surface states can be described by the equation:

$$E(k) = E_0 + \frac{\hbar^2 k^2}{2m^*} \quad (1)$$

where $E(k)$ is the energy of the electrons as a function of the wave vector k, E_0 is the energy at the minimum of the parabola, $\hbar$ is the reduced Planck's constant, and m^* is the effective mass of the electrons.

By fitting the parabolic dispersion using eq 1, the effective mass of electrons on both the pristine Au(111) surface and the $CoCl_2$-covered regions can be determined (see Figure 3). The effective mass for the clean Au(111) surface was determined at $m^*_{Au(111)} = 0.29m_e$ (see Figure S10), while for the $CoCl_2$-covered regions, it amounted to $m^*_{CoCl_2/Au(111)} = 0.32m_e$. This slight increase in effective mass in the $CoCl_2$-covered regions suggests that the $CoCl_2$ film introduces minimal scattering or interaction effects, maintaining the nearly free-electron-like nature of the surface state.

Another feature of interest visible only in the positive bias voltage range in Figure 3 is denoted by the violet dashed lines at ±0.15 Å^{-1} and appears to be nondispersive. This feature has been previously interpreted as resulting from gold bulk state electrons contributing to the local density of states.[34] Such nondispersive behavior, especially in the energy range above the Fermi level, contrasts with expectations from the projected band structure of bulk gold. The anomaly is likely due to differing inelastic relaxation rates for electron states above and below the Fermi level, which may cause a constant wave vector for bulk state electrons above the Fermi level.[34] The feature is very weak, likely due to tunneling through the $CoCl_2$ film, although alternative origins cannot be ruled out.

Once the structural and electronic properties of this single $CoCl_2$ layer are experimentally determined, we proceed to study its magnetic character. $CoCl_2$'s magnetic properties were measured via XAS/XMCD using circularly polarized synchrotron X-ray radiation. In contrast to conventional sample preparation, different coverages were all achieved on a single sample producing a gradient by systematically positioning a shutter across the evaporation beam, effectively covering distinct portions of the surface (see Figure S2 and Methods Section). Figure 4 shows measurements of $CoCl_2$ at different coverages (0.4, 1.1, and 1.4 ML) under both normal (NI) and grazing (GI) X-ray beam incidence. Upon examining the XAS spectra shown in Figure 4a and, in particular, the magnetization loop illustrated in Figure 4c, it becomes immediately apparent that the easy axis in $CoCl_2$ lies in the plane, signaling in-plane magnetization. Under grazing incidence, the magnetization loop achieves full saturation at magnetic field strengths below 1 T. Conversely, in normal incidence, the magnetization loop is practically a straight line with a shallow slope, failing to saturate even at 6 T. Since the NI measurements show no evidence of saturation at 6 T, the anisotropy field can be estimated extrapolating the NI and GI magnetization curves to their point of intersection. This leads to a saturation field of 31.4 T and corresponds to an anisotropy energy of 1.6 meV per Co atom ($H{\cdot}\mu_{at}/2 = E_a$,[36] where we use a spin atomic moment μ_{at} of 1.81 μ_B). It compares well to the value obtained for the monolayer $CoCl_2$ by the DFT calculations (0.7 meV[31]). On the other hand, much weaker anisotropy fields of 3 and 0.5

https://doi.org/10.1021/acsnano.5c02175
ACS Nano 2025, 19, 20693−20701

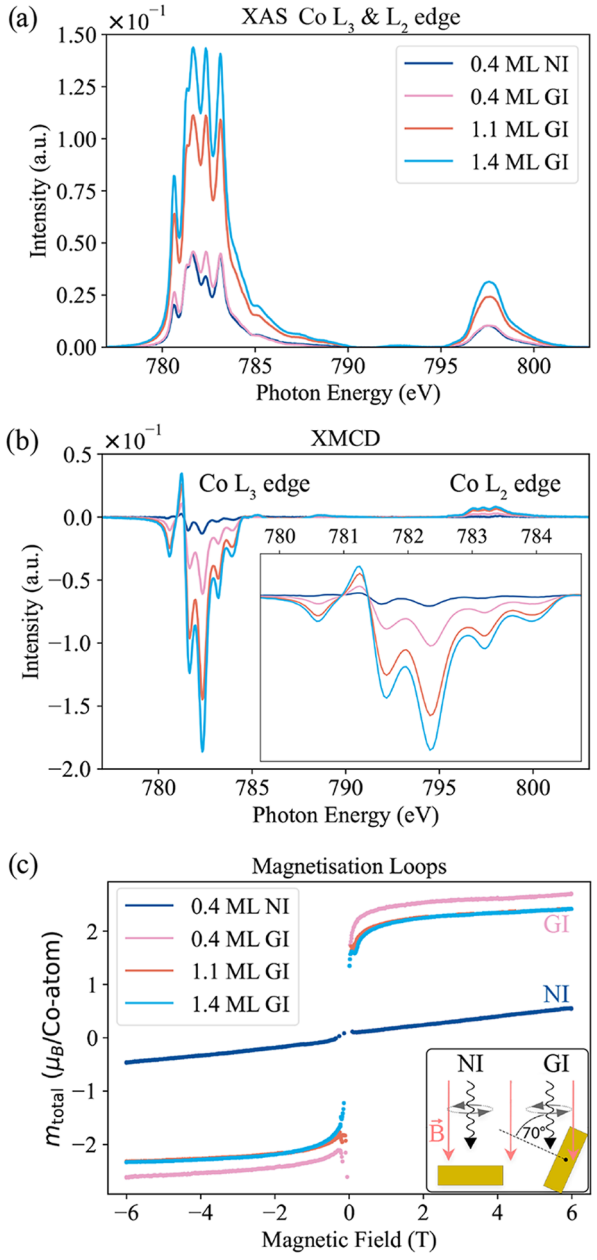

Figure 4. Magnetic characterization of $CoCl_2$ on Au(111). (a) XAS and (b) XMCD spectra measured at 2 K with an applied field of 6 T measured at the Co L_3- and L_2-edge in NI (normal incidence, 0°) and GI (grazing incidence, 70°) are displayed for different coverages of $CoCl_2$ on Au(111). The XMCD spectra are scaled to the peak height of the average XAS spectra. (c) Magnetization loops measured at the L_3-edge, for the 0.4 ML sample in NI and GI and the 1.1 and 1.4 ML sample in GI. All artificial spikes around 0 T have been removed because fluctuations in the magnetic field or alignment imperfections near zero can cause inconsistencies in total-electron-yield (TEY) measurements.

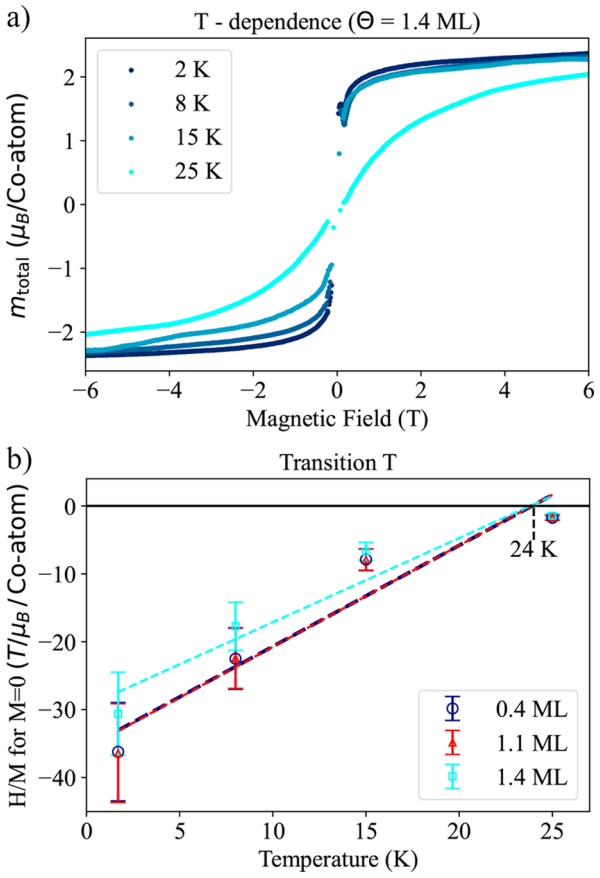

Figure 5. (a) Temperature-dependent magnetization loops of the 1.4 ML $CoCl_2$ sample. Notice how the curves shift from resembling an almost step function to an S-shaped pattern as the temperature increases. (b) Linear regression of the points obtained via the temperature-dependent magnetization loops and Arrott plots (see Figure S13) at each system temperature (1.7, 8, 15, 25 K). The intersect of the linear regression with the *x*-axis at 24 K denotes the transition temperature from a ferromagnetic to a paramagnetic order. The 0.4 and 1.1 ML linear regressions coincidentally overlap.

T were found for the Ising-type ferromagnets CrI_3 and $CrBr_3$, respectively.[10,37,38] This high saturation field indicates a robust in-plane anisotropy, emphasizing the distinctive magnetic behavior of $CoCl_2$ compared with other TMDH.[16,19] Another key feature can be inferred from the XAS and XMCD peak structure in Figure 4a,b: The multiplet splitting at the Co L_3- and L_2-edge remains consistent with increasing coverage. This feature suggests a uniform and single-phase growth that maintains its characteristics between the first and second monolayer and is not affected by the theoretically predicted antiferromagnetic coupling between layers.[31] This also points to minimal interactions between the Au(111) substrate and $CoCl_2$, further reinforcing the conclusions about the weak interlayer forces and strong intralayer stability discussed previously.

After investigating the behavior of $CoCl_2$ for different thicknesses, the temperature-dependent magnetization loops were explored. This involved incrementally adjusting the system's set point temperature, while the magnetic field strength was varied from −6 to +6 T and back. Four distinct temperatures were studied: 2, 8, 15, and 25 K. In Figure 5a, a noticeable and gradual transition is observed in the magnetization loop of 1.4 ML $CoCl_2$ from an almost step-like profile at 2 K to a flatter, s-shaped curve at 25 K (T-dependent loops at 0.4 and 1.1 ML are plotted in Figure S13). We used Arrott plot analysis to determine the critical temperature as in refs 17,39 and found a transition temperature of 24 K. Below the transition temperature, $CoCl_2$ shows ferromagnetic properties, with the magnetic moments aligning to produce a step-like

https://doi.org/10.1021/acsnano.5c02175
ACS Nano 2025, 19, 20693−20701

profile in the magnetization loop. As the temperature rises above 24 K, $CoCl_2$ becomes paramagnetic, indicated by a more gradual, s-shaped magnetization curve. This shift reflects the loss of magnetic order due to thermal excitation, causing the magnetic moments to orient randomly without any long-range alignment.

We calculate spin and orbital magnetic moments via sum rules analysis (Figure S13): Halogens are generally considered to create a weak crystal field, thus leading only to a weak energy difference between e_g and t_{2g},[40] leading predominantly to a high-spin configuration. Co^{2+} being a $3d^7$ transition metal would, according to Hund's rules, have a magnetic moment of $3\mu_B$ per Co atom. At the lowest temperature (2 K), the calculated magnetic moments of $CoCl_2$ for all measured coverages are lower than those predicted by Hund's rules (see Table 1). This was observed for the whole family of TMDH,[16,19] besides $NiBr_2$ on Au(111).[17]

Table 1. Magnetic Moments Measured by XMCD for Different Coverages (Θ) at T = 2 K and B = 6 T[a]

		μ (μ_B/Co atom)			
		NI	GI		
Θ (ML)	T (K)	m_{tot}	$m_{s,eff}$	m_l	m_{tot}
0.4	2	0.52	1.81	0.91	2.72
	8		1.76	0.89	2.65
	15		1.79	0.87	2.66
	25		1.34	0.76	2.10
1.1	2	0.52	1.60	0.81	2.41
	8		1.63	0.78	2.41
	15		1.62	0.76	2.38
	25		1.41	0.67	2.08
1.4	2	0.54	1.60	0.83	2.43
	8		1.53	0.79	2.32
	15		1.52	0.77	2.29
	25		1.35	0.70	2.05

[a]The magnetic moments (μ) are calculated for the in-plane and out-of-plane measurements. The total magnetic moment m_{tot} per Co atom is the sum of the effective spin moment $m_{s,eff}$ and the orbital moment m_l. The measured moments are shown for NI and GI with an error of ±10%. More details about the procedure of sum rules analysis are available in Figure S13.

The reduced magnetic moments observed in $CoCl_2$ and other TMDHs could potentially be attributed to a combination of geometric and electronic factors. In $CoCl_2$, cobalt atoms are located in the center of an octahedral arrangement of chloride ions. Owing to its strong ionic nature, the cobalt-chloride distance is mostly determined by the size of the Cl^- anion. This could reduce the orbital overlap between the cobalt d-orbitals and chlorine p-orbitals, leading to a weaker crystal field. The presence of lattice distortions due to interactions with Au(111) might also affect the electronic configuration, potentially allowing for a mixture of high-spin and low-spin states. Deviations from a perfect octahedral symmetry can further split the t_{2g} and e_g orbitals into additional sublevels. These distortions could lead to partial quenching of the orbital magnetic moment, which, through spin−orbit coupling, can also reduce the effective spin magnetic moment. Both the quenching and the modified orbital environment could influence the magnetic anisotropy, as seen with the strong in-plane magnetization in $CoCl_2$. This suggests that the reduced magnetic moments in $CoCl_2$ and similar TMDHs could result from reduced orbital overlap, modified crystal field effects, altered electronic configurations, and inhomogeneities in the lattice.

CONCLUSIONS

$CoCl_2$ on Au(111) exhibits highly ordered growth with weak substrate interactions carpeting over Au(111) step edges, demonstrating a high intralayer stability. Similar to the bulk material, it shows a semiconducting behavior with a band gap of approximately 3.9 eV. Surprisingly, in-gap states near Fermi energy arising from interface interactions with gold were measured via STS, opening possible applications in interface engineering, tunable charge transport, or enhanced catalytic activity.

XAS and XMCD measurements also reveal a strong in-plane magnetic anisotropy and a high transition temperature of around 24 K from ferromagnetic to paramagnetic ordering. The magnetic moments are lower than predicted by Hund's rules, which may be attributed to geometric and electronic factors that lead to decreased orbital overlap, altered crystal field effects, changes in electronic configurations, and partial quenching of the magnetic moment. These findings offer new ways for tailoring magnetic properties through interface engineering or substrate choice. The unique combination of semiconducting behavior, interfacial gap states, and magnetic ordering positions $CoCl_2$ as a promising material for next-generation nanoscale devices. Applications in spintronics, magnetic sensors, or energy-efficient memory technologies are particularly compelling, given its potential for tunable electronic and magnetic properties.

METHODS

Cobalt dichloride ($CoCl_2$) films (submonolayer to multilayer) were grown on Au(111) using a Knudsen cell evaporator with quartz crucibles (Dodecon OMBE Source[41]). The evaporation was performed under ultra-high vacuum (UHV) conditions (evaporation pressure of 10^{-8}−10^{-9} mbar) at a temperature of roughly 400 °C. While $FeBr_2$ has been shown to grow with the substrate at room temperature,[16] slightly elevated substrate temperatures of roughly 100 °C were needed for ordered $CoCl_2$ growth, analogue to $FeCl_2$ and $NiCl_2$.[19] The amount of evaporated material was estimated via a quartz microbalance, while low-temperature scanning tunneling microscopy (LT-STM), X-ray photoelectron spectroscopy (XPS), and low-energy electron diffraction (LEED) were used as a cross-reference.

The purity of the anhydrous beads of $CoCl_2$ from Sigma-Aldrich used in the experiment was labeled at 99.9%[42] and the substrate cleaning process involved standard Ar^+ sputtering and annealing cycles at 720 K.

The $CoCl_2$ films (from 0.4 ML, 1.1, and 1.4 ML) used for XAS experiments were prepared consecutively on the same sample by incrementally adjusting a shutter across the Au(111) crystal at predefined intervals. This yields a sample with a gradient of coverage grown sequentially. A schematic representation is shown in Figure S2.

The magnetic characterization was performed at the DEIMOS beamline at the SOLEIL synchrotron with a degree of circular polarization of 98%.[43] The lowest achievable measurement temperature was 2 K[44] and higher system temperatures were attained through counter heating and thermostatization. The sample's circular dichroism was measured in normal incidence (NI) as well as in grazing incidence (GI ∼ 70°), as is shown in Figure 4, yielding information about the material's anisotropy and magnitude of the magnetic moment. Table 1 contains the magnetic moment values obtained from the sum rule analysis for the different sample coverages and temperatures are displayed.

https://doi.org/10.1021/acsnano.5c02175
ACS Nano 2025, 19, 20693−20701

Figure 4a shows the white line absorption spectra at the Co L_3- and L_2-edges of Co, averaged over both left and right circular polarizations. Figure 4b displays the corresponding XMCD spectra, and Figure 4c presents the magnetization loops measured at a beam energy of approximately 782.5 eV, where the XMCD signal reaches its maximum. The XAS spectra have been normalized to the pre-edge and a background subtraction has been performed.[45] The magnetization curves measured for different coverages at ≈2 K in the two different geometries were measured in total electron yield (TEY) mode and are scaled to the calculated expectation values of the total magnetic moment at 2 K and 6 T. As a result, the intensity values correspond to the projection of the total magnetic moment per Co atom in the direction of the X-ray beam under a 6 T magnetic field.

The STM experiments were performed with a Scienta-Omicron LT-STM at 4.3 K and 10^{-10} mbar base pressure.

The AFM experiments were performed with a SPECS Low-temperature Scanning Probe Microscope with Joule-Thompson stage at 1.4 K and a CO-functionalized tip with Kolibri sensor.[46] The base pressure was 10^{-10} mbar and Nanonis software was used.

The XPS measurements were carried out with a Phoibos 100 photoelectron spectrometer, using a nonmonochromatic Al Kα X-ray source. The energy resolution is 0.1 eV.

UHV conditions were preserved during all of the sample transfers (base pressure during the experiment was 10^{-10} mbar).

ASSOCIATED CONTENT

Supporting Information

The Supporting Information is available free of charge at https://pubs.acs.org/doi/10.1021/acsnano.5c02175.

Schematic Structure, Preparation of Wedged Sample, STM Length and Rotation Calibration, Large-Scale STM of 1−1.5 ML $CoCl_2$ Coverage, STS in the Second ML, Surface State Dispersion Calculation, FFT and Au(111) Dispersion, XPS Fitting Procedure and Parameters, XPS Co 2p, Cl 2p, Au 4s, and Survey Plot, LEED Series up to 3.2 ML, XAS Coverage Calibration, XMCD Sum Rule Analysis, Temperature-Dependent Magnetization Curves and Arrott Plots (PDF)

AUTHOR INFORMATION

Corresponding Authors

Samuel Kerschbaumer − *Centro de Física de Materiales (CSIC/UPV-EHU), 20018 Donostia-San Sebastián, Spain;* orcid.org/0000-0001-6099-2265; Phone: +34 943 01 5804; Email: kerschbaumersamuel@gmail.com

Celia Rogero − *Centro de Física de Materiales (CSIC/UPV-EHU), 20018 Donostia-San Sebastián, Spain;* orcid.org/0000-0002-2812-8853; Phone: +34 943 01 5804; Email: celia.rogero@ehu.eus

Authors

Sebastien Elie Hadjadj − *Centro de Física de Materiales (CSIC/UPV-EHU), 20018 Donostia-San Sebastián, Spain;* orcid.org/0000-0002-6045-574X

Andrea Aguirre-Baños − *Centro de Física de Materiales (CSIC/UPV-EHU), 20018 Donostia-San Sebastián, Spain*

Danilo Longo − *CIC nanoGUNE-BRTA, 20018 Donostia-San Sebastian, Spain*

Andrés Pinar Solé − *FZU − Institute of Physics of the Czech Academy of Sciences, Prague 6 CZ 16200, Czech Republic*

Oleksandr Stetsovych − *FZU − Institute of Physics of the Czech Academy of Sciences, Prague 6 CZ 16200, Czech Republic*

Adriana Elizabet Candia − *Centro de Física de Materiales (CSIC/UPV-EHU), 20018 Donostia-San Sebastián, Spain; Laboratorio de Microscopias Avanzadas (LMA), Universidad de Zaragoza, E-50018 Zaragoza, Spain*

Paula Angulo-Portugal − *Centro de Física de Materiales (CSIC/UPV-EHU), 20018 Donostia-San Sebastián, Spain;* orcid.org/0000-0002-1770-0025

David Caldevilla − *Centro de Física de Materiales (CSIC/UPV-EHU), 20018 Donostia-San Sebastián, Spain;* orcid.org/0009-0004-3542-3086

Fadi Choueikani − *Synchrotron SOLEIL, 91190 Saint-Aubin, France*

Martina Corso − *Centro de Física de Materiales (CSIC/UPV-EHU), 20018 Donostia-San Sebastián, Spain;* orcid.org/0000-0002-8592-1284

David Serrate − *Instituto de Nanociencia y Materiales de Aragón (INMA), CSIC-Universidad de Zaragoza, 50009 Zaragoza, Spain; Departamento de Física de la Materia Condensada, Universidad de Zaragoza, E-50009 Zaragoza, Spain;* orcid.org/0000-0002-3260-9641

Jorge Lobo-Checa − *Instituto de Nanociencia y Materiales de Aragón (INMA), CSIC-Universidad de Zaragoza, 50009 Zaragoza, Spain; Departamento de Física de la Materia Condensada, Universidad de Zaragoza, E-50009 Zaragoza, Spain;* orcid.org/0000-0003-2698-2543

Pavel Jelínek − *FZU − Institute of Physics of the Czech Academy of Sciences, Prague 6 CZ 16200, Czech Republic;* orcid.org/0000-0002-5645-8542

Maxim Ilyn − *Centro de Física de Materiales (CSIC/UPV-EHU), 20018 Donostia-San Sebastián, Spain;* orcid.org/0000-0002-4052-7275

Complete contact information is available at: https://pubs.acs.org/10.1021/acsnano.5c02175

Notes

The authors declare no competing financial interest.

ACKNOWLEDGMENTS

The authors gratefully acknowledge the financial support by the Spanish MCIU/AEI/10.13039/501100011033 and the European Union "NextGenerationEU"/PRTR (Grant Nos. PID2020-114252GB-I00, PID2022-140845OB-C6, PID2022-138750NB-C21, PID2022-138750NB-C22, PID2022-140845OB-C65, TED2021-132388B-C43, TED2021-130292B-C42, the scholarship PRE2020-093355, and the scholarship PRE-2021-1-0350), the Basque Government INKER EC-2024-1-0010, IT1591-22, from the regional Governments of Aragon (E12-23R), the Spanish Research Council CSIC through I-LINK C20002, and the IKUR Strategy (HPC-IA and QT 2023−2025) under the collaboration agreement between Ikerbasque Foundation, MPC, and DIPC on behalf of the Department of Education of the Basque Government. We also acknowledge the financial support of Czech Science Foundation GACR 20-13692X and CzechNanoLab Research Infrastructure supported by MEYS CR LM2023051. We further acknowledge the use of Servicio General de Apoyo a la Investigación-SAI and the Laboratorio de Microscopías Avanzadas of the Universidad de Zaragoza. We also thank beamline DEIMOS and Synchrotron Soleil for the opportunity of performing XAS/XMCD measurements. S.K. acknowledges funding of the Ph.D. fellowship from the

MPC Asociación. D.L. acknowledges the MSCA project QMOLESR (Project Number: 101064332).

REFERENCES

(1) Sethulakshmi, N.; Mishra, A.; Ajayan, P.; Kawazoe, Y.; Roy, A. K.; Singh, A. K.; Tiwary, C. S. Magnetism in two-dimensional materials beyond graphene. *Mater. Today* **2019**, *27*, 107−122.
(2) Khan, K.; Tareen, A. K.; Aslam, M.; Zhang, Y.; Wang, R.; Ouyang, Z.; Gou, Z.; Zhang, H. Recent advances in two-dimensional materials and their nanocomposites in sustainable energy conversion applications. *Nanoscale* **2019**, *11*, 21622−21678.
(3) Radisavljevic, B.; Radenovic, A.; Brivio, J.; Giacometti, V.; Kis, A. Single-layer MoS_2 transistors. *Nat. Nanotechnol.* **2011**, *6*, 147−150.
(4) Huang, B.; Clark, G.; Navarro-Moratalla, E.; Klein, D. R.; Cheng, R.; Seyler, K. L.; Zhong, D.; Schmidgall, E.; McGuire, M. A.; Cobden, D. H.; Yao, W.; Xiao, D.; Jarillo-Herrero, P.; Xu, X. Layer-dependent ferromagnetism in a van der Waals crystal down to the monolayer limit. *Nature* **2017**, *546*, 270−273.
(5) Li, H.; Ruan, S.; Zeng, Y. Intrinsic Van Der Waals Magnetic Materials from Bulk to the 2D Limit: New Frontiers of Spintronics. *Adv. Mater.* **2019**, *31*, No. 1900065, DOI: 10.1002/adma.201900065.
(6) Liu, Y.; Weiss, N. O.; Duan, X.; Cheng, H.-C.; Huang, Y.; Duan, X. Van der Waals heterostructures and devices. *Nat. Rev. Mater.* **2016**, *1*, 16042.
(7) Sulpizio, J. A.; Ilani, S.; Irvin, P.; Levy, J. Nanoscale Phenomena in Oxide Heterostructures. *Annu. Rev. Mater. Res.* **2014**, *44*, 117−149.
(8) Novoselov, K. S.; Mishchenko, A.; Carvalho, A.; Castro Neto, A. H. 2D materials and van der Waals heterostructures. *Science* **2016**, *353*, No. eaac9439.
(9) Hou, Y.; Kim, J.; Wu, R. Magnetizing topological surface states of Bi_2Se_3 with a CrI_3 monolayer. *Sci. Adv.* **2019**, *5*, No. eaaw1874, DOI: 10.1126/sciadv.aaw1874.
(10) McGuire, M. Crystal and Magnetic Structures in Layered, Transition Metal Dihalides and Trihalides. *Crystals* **2017**, *7*, 121.
(11) Nguyen, T. P. T.; Yamauchi, K. Goodenough−Kanamori−Anderson Rules in 2D Magnet: A Chemical Trend in $M\,Cl_2$ with M = V, Mn, and Ni. *J. Phys. Soc. Jpn.* **2024**, *93*, 034710.
(12) Wu, D.; Han, X.; Wu, C.; Song, Y.; Li, J.; Wan, Y.; Wu, X.; Tian, X. Two-Dimensional Transition Metal Boron Cluster Compounds (MBnenes) with Strain-Independent Room-Temperature Magnetism. *J. Phys. Chem. Lett.* **2024**, *15*, 1070−1078.
(13) Wu, D.; Zhuo, Z.; Lv, H.; Wu, X. Two-Dimensional $Cr_2X_3S_3$ (X = Br, I) Janus Semiconductor with Intrinsic Room-Temperature Magnetism. *J. Phys. Chem. Lett.* **2021**, *12*, 2905−2911.
(14) Gibertini, M.; Koperski, M.; Morpurgo, A. F.; Novoselov, K. S. Magnetic 2D materials and heterostructures. *Nat. Nanotechnol.* **2019**, *14*, 408−419.
(15) Gong, C.; Li, L.; Li, Z.; Ji, H.; Stern, A.; Xia, Y.; Cao, T.; Bao, W.; Wang, C.; Wang, Y.; Qiu, Z. Q.; Cava, R. J.; Louie, S. G.; Xia, J.; Zhang, X. Discovery of intrinsic ferromagnetism in two-dimensional van der Waals crystals. *Nature* **2017**, *546*, 265−269.
(16) Hadjadj, S. E.; González-Orellana, C.; Lawrence, J.; et al. Epitaxial Monolayers of the Magnetic 2D Semiconductor $FeBr_2$ Grown on Au(111). *Chem. Mater.* **2023**, *35*, 9847−9856.
(17) Bikaljević, D.; González-Orellana, C.; Peña-Díaz, M.; et al. Noncollinear Magnetic Order in Two-Dimensional $NiBr_2$ Films Grown on Au(111). *ACS Nano* **2021**, *15*, 14985−14995.
(18) Cai, S.; Yang, F.; Gao, C. $FeCl_2$ monolayer on HOPG: art of growth and momentum filtering effect. *Nanoscale* **2020**, *12*, 16041−16045.
(19) Aguirre, A.; Pinar Solé, A.; Soler Polo, D.; et al. Ferromagnetic Order in 2D Layers of Transition Metal Dichlorides. *Adv. Mater.* **2024**, *36*, 2402723.
(20) Wang, Q. H.; Kalantar-Zadeh, K.; Kis, A.; Coleman, J. N.; Strano, M. S. Electronics and optoelectronics of two-dimensional transition metal dichalcogenides. *Nat. Nanotechnol.* **2012**, *7*, 699−712.
(21) Wang, Q. H.; Bedoya-Pinto, A.; Blei, M.; et al. The Magnetic Genome of Two-Dimensional van der Waals Materials. *ACS Nano* **2022**, *16*, 6960−7079.
(22) Xue, Y.; Liu, H.; Zhang, Y.; Lin, S.; Lau, S. P. van der Waals epitaxial growth and high-temperature ferrimagnetism in ultrathin crystalline magnetite (Fe_3O_4) nanosheets. *J. Mater. Chem. C* **2022**, *10*, 7058−7065.
(23) Park, J.-H.; Kapur, P.; Saraswat, K. C.; Peng, H. A very low temperature single crystal germanium growth process on insulating substrate using Ni-induced lateral crystallization for three-dimensional integrated circuits. *Appl. Phys. Lett.* **2007**, *91*, No. 143107, DOI: 10.1063/1.2793183.
(24) Wang, M.-C.; Chang, C.-R. Goodenough-Kanamori-Anderson Rules in $CrI_3/MoTe_2/CrI_3$ Van der Waals Heterostructure. *J. Electrochem. Soc.* **2022**, *169*, 053507.
(25) Barreda-Argüeso, J. A.; Nataf, L.; Aguado, F.; Hernández, I.; González, J.; Otero-de-la Roza, A.; Luaña, V.; Jia, Y.; Jin, C.; Kim, B.; Kim, K.; Min, B. I.; Heribert, W.; Jephcoat, A. P.; Rodríguez, F. Pressure-induced spin transition and site-selective metallization in $CoCl_2$. *Sci. Rep.* **2019**, *9*, No. 5448, DOI: 10.1038/s41598-019-41337-4.
(26) Zhang, L.; Dong, J.; Ding, F. Strategies, Status, and Challenges in Wafer Scale Single Crystalline Two-Dimensional Materials Synthesis. *Chem. Rev.* **2021**, *121*, 6321−6372.
(27) Hernández-Rodríguez, I.; García, J. M.; Martín-Gago, J. A.; de Andrés, P. L.; Méndez, J. Graphene growth on Pt(111) and Au(111) using a MBE carbon solid-source. *Diamond Relat. Mater.* **2015**, *57*, 58−62.
(28) Materials Project 2024 http://www.materialsproject.org.
(29) *Handbook of X-ray Photoelectron Spectroscopy: A Reference Book of Standard Spectra for Identification and Interpretation of XPS Data*; Moulder, J. F.; Chastain, J., Eds.; Perkin-Elmer Corporation, 1992.
(30) Torun, E.; Sahin, H.; Singh, S. K.; Peeters, F. M. Stable half-metallic monolayers of $FeCl_2$. *Appl. Phys. Lett.* **2015**, *106*, No. 192404, DOI: 10.1063/1.4921096.
(31) Botana, A. S.; Norman, M. R. Electronic structure and magnetism of transition metal dihalides: Bulk to monolayer. *Phys. Rev. Mater.* **2019**, *3*, 044001.
(32) Liu, H.; Wang, A.; Zhang, P.; Ma, C.; Chen, C.; Liu, Z.; Zhang, Y.-Q.; Feng, B.; Cheng, P.; Zhao, J.; Chen, L.; Wu, K. Atomic-scale manipulation of single-polaron in a two-dimensional semiconductor. *Nat. Commun.* **2023**, *14*, No. 3690, DOI: 10.1038/s41467-023-39361-0.
(33) Prayitno, T. B.; Budi, E.; Fahdiran, R. Influence of LDA+U on band dispersion in monolayer MCl_2 (M: Fe, Co). *J. Phys.: Conf. Ser.* **2021**, *2019*, 012074.
(34) Schouteden, K.; Lievens, P.; Van Haesendonck, C. Fourier-transform scanning tunneling microscopy investigation of the energy versus wave vector dispersion of electrons at the Au(111) surface. *Phys. Rev. B* **2009**, *79*, 195409.
(35) Hasegawa, Y.; Avouris, P. Direct observation of standing wave formation at surface steps using scanning tunneling spectroscopy. *Phys. Rev. Lett.* **1993**, *71*, 1071−1074.
(36) Skomski, R.; Manchanda, P.; Kashyap, A. *Handbook of Magnetism and Magnetic Materials*; Coey, J. M. D.; Parkin, S. S., Eds.; Springer International Publishing: Cham, 2021; pp 103−185.
(37) McGuire, M. A.; Dixit, H.; Cooper, V. R.; Sales, B. C. Coupling of Crystal Structure and Magnetism in the Layered, Ferromagnetic Insulator CrI3. *Chem. Mater.* **2015**, *27*, 612−620.
(38) Hansen, W. N. Some Magnetic Properties of the Chromium (III) Halides at 4.2 K. *J. Appl. Phys.* **1959**, *30*, S304−S305.
(39) Lin, G. T.; Zhuang, H. L.; Luo, X.; Liu, B. J.; Chen, F. C.; Yan, J.; Sun, Y.; Zhou, J.; Lu, W. J.; Tong, P.; Sheng, Z. G.; Qu, Z.; Song, W. H.; Zhu, X. B.; Sun, Y. P. Tricritical behavior of the two-dimensional intrinsically ferromagnetic semiconductor CrGeTe 3. *Phys. Rev. B* **2017**, *95*, 245212.
(40) Atkins, P. *Shriver and Atkins' Inorganic Chemistry*; OUP: Oxford, 2010; pp 473−487.
(41) Dodecon 4x OMBE Source 2024 https://dodecon.de/4xOMBE.html.
(42) Sigma-Aldrich. Cobalt(II) Chloride 2024 https://www.sigmaaldrich.com/ES/es/product/aldrich/449776.

https://doi.org/10.1021/acsnano.5c02175
ACS Nano 2025, 19, 20693−20701

(43) Ohresser, P.; Otero, E.; Choueikani, F.; Stanescu, S.; Deschamps, F.; Ibis, L.; Moreno, T.; Polack, F.; Lagarde, B.; Marteau, F.; Scheurer, F.; Joly, L.; Kappler, J.-P.; Muller, B.; Sainctavit, P. Polarization characterization on the DEIMOS beamline using dichroism measurements. *J. Phys.: Conf. Ser.* **2013**, *425*, 212007.
(44) Ohresser, P.; Otero, E.; Choueikani, F.; et al. DEIMOS: A beamline dedicated to dichroism measurements in the 350−2500 eV energy range. *Rev. Sci. Instrum.* **2014**, *85*, 013106.
(45) Baek, S.-J.; Park, A.; Ahn, Y.-J.; Choo, J. Baseline correction using asymmetrically reweighted penalized least squares smoothing. *Analyst* **2015**, *140*, 250−257.
(46) Torbrügge, S.; Schaff, O.; Rychen, J. Application of the KolibriSensor to combined atomic-resolution scanning tunneling microscopy and noncontact atomic-force microscopy imaging. *J. Vac. Sci. Technol. B* **2010**, *28*, C4E12−C4E20.

https://doi.org/10.1021/acsnano.5c02175
ACS Nano 2025, 19, 20693−20701